Adsorption of direct red 79 in wastewater on $Fe_2Fe_{1-X}Mn_XO_4$ (x = 0-1) nanoparticles prepared by co-precipitation method

Pham Hoai Linh[1], Nguyen Quoc Dung[2, *], Nguyen Van Khien[3]

[1]*Institute of Materials Science, Vietnam Academy of Science and Technology, 18 Hoang Quoc Viet, Cau Giay, Ha Noi, Viet Nam*

[2]*Faculty of Chemistry, Thai Nguyen University of Education, No. 20, Luong Ngoc Quyen, Thai Nguyen City, Thai Nguyen, Viet Nam*

[3]*TNU-University of Sciences, Tan Thinh Ward, Thai Nguyen City, Thai Nguyen, Viet Nam*

[*]Emails: *dungnq@tnue.edu.vn*

Abstract. Magnetic spinel ferrite nanoparticles $Fe_2Fe_{1-x}Mn_xO_4$ were synthesized by a simple co-precipitation method. The morphology and structures of the synthesized samples were characterized by X-ray diffraction (XRD), field-emission scanning electron microscope (FE-SEM), Raman spectroscopy, and infrared spectroscopy (FTIR). The magnetic properties of the materials were studied using VMS measurement. The results showed that the spinel ferrite nanoparticles formed a single phase of packed face-centered cubic spinel structure. When replacing Mn^{2+} ions with Fe^{2+}, the crystal structure shifted from the Fe_3O_4 crystal structure to the $MnFe_2O_4$ crystal structure assigned with an increased lattice constant from 6.30 nm to 26.33 nm. Raman and FTIR spectrum analysis showed that when replacing Mn^{2+} ions with Fe^{2+}, the Mn-O and Fe-O bonds changed significantly. Specifically, the intensity of the Raman spectrum's reflection and the FTIR spectrum's absorption decreased gradually. All the samples exhibited uniform spherical shapes, and particle size varied from 9.8 nm to 30 nm, depending strongly on the substituted concentration. The magnetization curves confirm the soft ferromagnetic behavior with close superparamagnetic properties of $Fe_2Fe_{1-x}Mn_xO_4$ nanoparticles. The material used to study the adsorption of Direct Red 79 (DR79) in water has good adsorption capacity. The adsorption process obeys pseudo-second-order kinetics and also shows compliance with Langmuir, Freundlich and Temkin isotherms.

Keywords: spinel ferrite, magnetization, adsorption, Direct Red 79

Classification numbers: 2.2.1, 2.5.1, 3.4.2.

1. INTRODUCTION

Along with the development of the economy and the needs of life, the textile and garment industry has developed rapidly and has become an important and large-scale industry in Viet Nam and the world. Weaving and dyeing technology has developed, but the main source of raw

materials is still ordinary cellulose fibers. The dyeing process usually uses colorants covalently bonded to the hydroxyl group in the cellulose polymer molecule [1]. However, the water used to clean the fabric after use contains many dyes and toxic chemical additives that strongly affect human health and the environment [2]. Thus, water treatment before discharging into the environment has become an urgent issue that has attracted scientists' attention [3]. Currently dyes are divided into many types including direct, basic, acid, reactive, metal complex, and solubilized vat. Among them, direct dyes own one or more azo groups and are commonly used for coloring and painting. They have a much larger molecular weight than other types. They are often toxic, irritating to the skin, inflammatory, mutagenic, and carcinogenic. About 80 % of direct dyes are azo that need to be removed from wastewater [4]. Direct Red 79 is one of the direct dyes [5 - 7]. Studying its adsorption also predicts the adsorption of other direct dyes. There are many physical, chemical, and biological methods to remove dyes from wastewater, such as coagulation, membrane filtration, precipitation, electrochemical techniques, hydrolysis, photocatalysis, and adsorption. Adsorption is a popular method due to its low cost and high efficiency [8].

With the development of nanotechnology, using nanoadsorbents offers many advantages for the adsorption technique, such as enhanced removal efficiency, which is easy to use on a larger scale [9]. There are different types of adsorbent nanomaterials used in wastewater treatment, such as carbon nanotubes [10], graphene [11], metal oxides [12], etc. To increase the adsorption capacity, the recovery of adsorbents is increasingly interested in research. One of the ways to recover adsorbent material quickly is to take advantage of the material's magnetic properties. Previous studies showed that nanostructured magnetic materials, especially magnetic nanomaterials that belonged to the spinel structure family were highly effective in removing pollutants in water [13]. Due to their highly flexible surface, spinel ferrite nanomaterials readily interact with molecules and pollutant ions. Under an external magnetic field, these materials are easily separated, recovered, and reused for a long time after adsorbing contaminants. Spinel ferrite magnetic materials are an important class of composite metal oxides containing ferric ions. They have a a closely packed face-centered cubic structure that is formed by oxygen anions, and the smaller metal cations (M^{2+} and Fe^{3+}) occupied the hole positions: tetrahedral and octahedral oxygen coordination (termed as A and B sites, respectively) with the general structural formula $[M^{2+}]_A[Fe_2^{3+}]_BO_4$ (where M = Mg^{2+}, Co^{2+}, Ni^{2+}, Zn^{2+}, Fe^{2+}, Mn^{2+}, etc.) [14]. According to a recent review by Yun [15], iron oxide nanoparticles, Fe_3O_4, have been traditionally used for water treatment applications with the ability to adsorb and remove heavy metals such as As, Cu, Pb, Se up to 99 % [16, 17]. However, in low pH environments, Fe_3O_4 nanoparticles are subjected to phase changes which significantly influence the magnetic characteristics of the particles and lead to a change in the pollutant removal performance. In order to overcome this problem, recent attempts have focused on using the substituted-spinel ferrite $M_xFe_{3-x}O_4$ (M = Mn, Zn, Mg, etc.) for contaminant removal [18]. In fact, the most interesting characteristic of spinel ferrite materials is that their structure and magnetic properties depend strongly on the cation distributions and super-exchange interaction between cations at the A site and cations at the B site. Therefore, by doping or substituting other ions such as Co^{2+}, Mn^{2+}, Zn^{2+}, Ni^{2+} to MFe_2O_4 spinel materials, different spinel structures (invert spinel, normal spinel, and mixed spinel) can be obtained [19]. This flexibility may result in significant changes in the magnetic properties and adsorption characteristics [15, 19].

In this study, $Fe_2Fe_{1-x}Mn_xO_4$ materials were used for the first time to study the adsorption of DR79 from aqueous solution. The effects of the initial pH medium, amount of adsorbent,

initial concentration, adsorption time, and temperature were investigated. The adsorption kinetic models and isotherm equations were analyzed and calculated based on the survey data.

2. MATERIALS AND METHODS

2.1. Materials

Metal salts and NaOH were purchased from Sigma-Aldrich. All chemicals used in this study were of analytical grade and used directly without further purification. $Mn_xFe_{3-x}O_4$ (x=0-1) nanoparticles were synthesized by a simple co-precipitation method. Typically, a mixture of metal precursors $MnCl_2.4H_2O$ and $FeCl_2.4H_2O$ with various molar ratios of Fe^{2+}/Mn^{2+} corresponding to x = 0, 0.2, 0.4, 0.6, 0.8, 1 was dissolved in 20 mL of H_2O using a magnetic stirrer. Then, the mixed solution was added to a solution of $FeCl_3.6H_2O$ according to the molar ratio (Mn^{2+}/Fe^{2+}): Fe^{3+} = (1):2. The mixed metal salt solution was added dropwise to a NaOH solution under a magnetic stirrer. The reaction was maintained at 60 ^{o}C for 1 hour. After that, the dark precipitation was separated by a permanent magnet and washed several times until pH = 7, and then dried in an oven at 60 ^{o}C for 24 hours.

2.2. Methods

Characterization

The crystal structure and phase structure, morphology, particle size, and chemical structure of the synthesized samples were characterized by X-ray diffraction analysis (XRD-Bruker D8 Advance), field-emission scanning electron microscopy (FESEM, S-4800, Hitachi), FTIR spectroscopy (Nicolet Nexus 670 FTIR), and Raman spectra (XploRA, Horiba). The magnetic properties were observed on magnetization plots through a homemade VSM.

Adsorption isotherms

The effects of pH, adsorbent dose, and adsorption time on the adsorption of DR79 were investigated. The adsorption medium was pH-adjusted water by adding 0.1 M NaOH or 0.1 M HNO_3. The adsorption process was accelerated by shaking at 3000 rpm. After adsorption, the samples were centrifuged at 5000 rpm for 10 min. The concentration of DR79 was determined using a UV-1700 spectrophotometer. The maximum optical absorption of DR79 was at 508 nm.

2.3. Theoretical background

Adsorption efficiency: Removal (%), adsorption capacity at equilibrium: q_e (mg/g), and adsorption capacity at time t: q_t (mg/g) were calculated according to the following equations:

$$\text{Removal (\%)} = \frac{C_0 - C_e}{C_0} \tag{1}$$

$$q_e = \frac{(C_0 - C_e)V}{m} \tag{2}$$

$$q_t = \frac{(C_0 - C_t)V}{m} \tag{3}$$

where, C_0, C_e, and C_t (mg/L) are the concentrations of the dye at the initial time, at equilibrium, and at any moment, respectively; V (L) is the volume of solution; m (g) is the amount of adsorbent.

Langmuir, Freundlich, and Temkin adsorption isotherms are commonly used to study adsorption [20, 21]. The Langmuir model is a homogeneous monolayer adsorption model according to the following equation:

$$\frac{C_e}{q_e} = \frac{1}{q_{max}K_L} + \frac{C_e}{q_{max}}$$

(4)

q_{max} và K_L are constants of the Langmuir model, q_{max} is maximum adsorption capacity. q_{max} and K_L are determined from the slope and intercept of the plot $\frac{C_e}{q_e}$ vs C_e.

The Freundlich model describes a heterogeneous adsorption process:

$$\ln q_e = \ln K_F + \frac{1}{n}\ln C_e$$

(5)

where n and K_F are constants, K_F is Freundlich constant, n and K_F are determined from the slope and intercept of the plot $\ln q_e$ versus $\ln C_e$.

The Temkin model describes a linear dependence:

$$q_e = \frac{RT}{b_t}\ln A_t + \frac{RT}{b_t}\ln C_e$$

(6)

where, A_t (L/g) and b_t (J/mol) are Temkin constants. T and R are the absolute temperature (K) and universal gas constant [8.314 J/(mol K)], respectively. A_t and b_t are determined from the slope and intercept of the plot q_e versus $\ln C_e$.

The adsorption kinetics was investigated according to the following models: Pseudo-first-order, Pseudo-second-order, Elovich, and Intra-particle diffusion model mentioned in reference [22].

The pseudo-first-order kinetic model (rate constant: k_1) with a linear expression is shown as follows:

$$\ln(q_e - q_t) = \ln q_e - k_1 t$$

(7)

The pseudo-second-order kinetic model (rate constant: k_2) with a linear expression is shown as follows:

$$\frac{t}{q_t} = \frac{1}{k_2 q_e^2} + \frac{1}{q_e}t$$

(8)

The Elovich model shows the nature of chemisorption. It allows for predicting the activation energy, deactivation, and diffusion processes of the system:

$$q_t = \frac{1}{\beta}\ln(\alpha\beta) + \frac{1}{\beta}\ln t$$

(9)

where, α [mg/(g min] is the initial adsorption rate, and β is the desorption constant.

The intra-particle diffusion model is used to study the rate-limiting step during adsorption with a linear expression:

$$q_t = K_p\sqrt{t} + C$$

(10)

where K_p is a rate constant, and C is the boundary layer thickness.

3. RESULTS AND DISCUSSION

3.1. Morphology and structure of materials

The crystalline phase structure of the samples was demonstrated by X-ray diffraction (XRD) measurement. Figure 1 shows the XRD patterns of Fe_3O_4, $MnFe_2O_4$ and $Fe_2Fe_{1-x}Mn_xO_4$ (x = 0.2; 0.4; 0.6; 0.8).
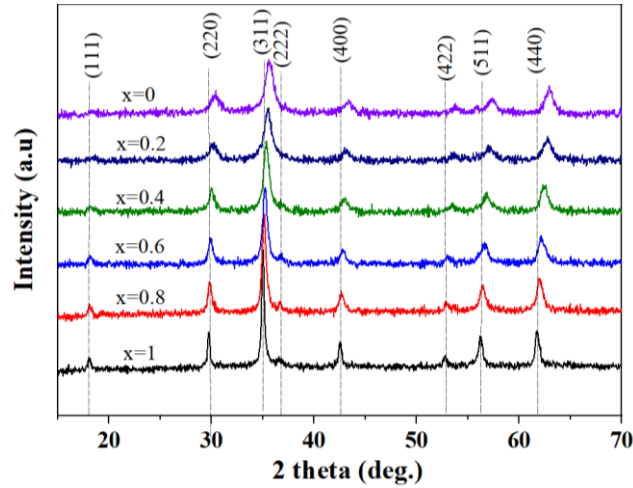
Figure 1. XRD patterns of Fe_3O_4, Fe_2MnO_4 and $Fe_2Fe_{1-x}Mn_xO_4$.

From Figure 1, it can be seen that all the samples exhibit the characteristic peaks of the face-centered cubic structure belonging to spinel ferrite materials with the peaks at around 18.32^o, 30.14^o, 35.50^o, 43.150^o, 53.54^o, and 57.07^o corresponding to the (111), (220), (311), (400), (422), (511), and (440) planes. For the samples with x = 1, the peaks' positions are consistent with the structure of the $MnFe_2O_4$ material (card of JCPDS No.10-0319) [23]. For the samples with x = 0, the XRD pattern clearly shows the typical peaks of Fe_3O_4 structure (well-matched with JCPDS 71-6336) without any strange impurity phase, confirming the single phase [24, 25]. For the substituted $Fe_2Fe_{1-x}Mn_xO_4$ samples, the diffraction peaks gradually shift to the 2θ angular position of the $MnFe_2O_4$ material when increasing the concentration of the substituted Mn^{2+} ions to Fe^{2+} in the Fe_3O_4 crystal. The crystal size of the sample system can be determined by Scherrer equation [26].

$$d_{\text{hkl}} = \frac{0,94.\lambda}{\beta.\cos\theta} \tag{11}$$

Table 1. XRD, TEM and magnetic properties analysis data for the synthesized samples, a (lattice parameter); d_{311} (d-spacing of 311 planes); d_{XRD} (crystalline size); d_{SEM} (particle size); M_S (saturation magnetization); H_C (coercivity).

Substituted concentrations	a (Å)	d_{311} (Å)	d_{XRD} (nm)	d_{SEM} (nm)	Ms (emu/g)	Hc (Oe)
x = 1	8.4977	30.8	26.325	30.2	41	58
x = 0.8	8.4716	15.5	13.775	18.1	47	1
x = 0.6	8.4478	19.5	12.175	17.6	58	2
x = 0.4	8.4119	10.4	10.6975	14.7	67	7
x = 0.2	8.3808	6.3	10.63	11.6	65	18
x = 0	8.3525	5.98	6.295	9.8	74	76

From Table 1, it can be seen that lattice parameters, including lattice constant and d-spacing of Fe_3O_4 nanoparticles increase with an increase in Mn^{2+} substituted concentration. From Figure 2, it can be seen that the lattice constant is increasing linearly with the substituted concentration. This increase could be originated from the ionic radius of Mn^{2+} (0.081 Å) being larger than that of Fe^{2+} (0.074 Å). When Mn^{2+} ions took the place of Fe^{2+} ions in the crystal, a lattice expansion occurred. The shifting of diffraction peaks and the change of the crystal parameters in the substituted samples confirm the successful replacement of Mn^{2+} for Fe^{2+} in the Fe_3O_4 nanoparticles by a simple co-precipitation method.
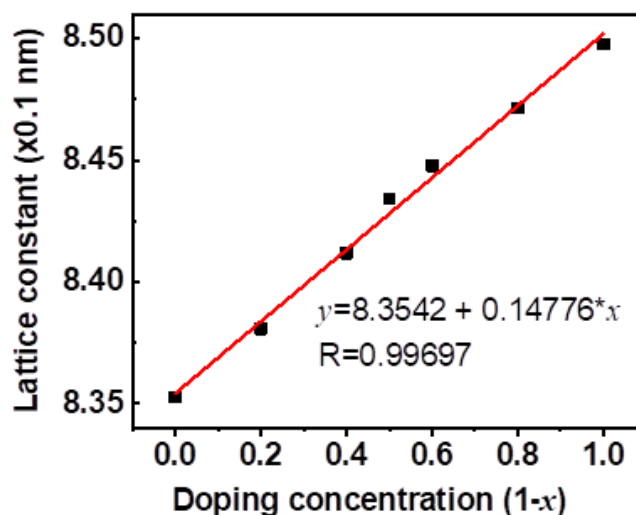
Figure 2. Dependence of lattice constant on the doping concentration.
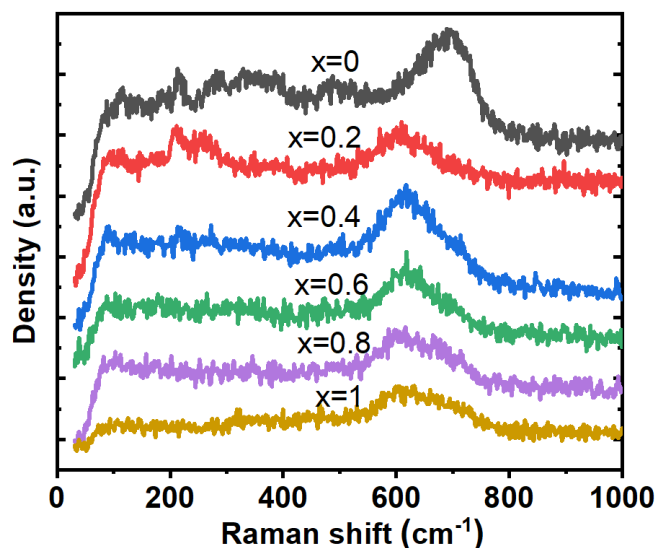
Figure 3. Raman spectra of $Fe_2Fe_{1-x}Mn_xO_4$.

Figure 3 presents the Raman spectra of the $Fe_2Fe_{1-x}Mn_xO_4$ (x = 0-1) samples in a wavelength range from 0 to 1000 cm^{-1}. The broad peak centered at 664 cm^{-1} was attributed to A1g mode corresponding to the symmetric stretch of oxygen atoms along Fe–O in Fe_3O_4 NPs

[27]. When Fe^{2+} ions were substituted by Mn^{2+} ions in the crystal, the characteristic peaks of the Fe-O bond shifted clearly to the low wavelength. These results confirm again that Mn^{2+} was successfully incorporated into the Fe_3O_4 lattice

To fully understand the chemical structure of the synthesized samples, the FT-IR spectra of $Fe_2Fe_{1-x}Mn_xO_4$ (x = 0-1) samples were performed and are shown in Figure 4. All samples exhibit the major absorption bands centered at 3380 cm^{-1} and 2350 cm^{-1} related to the O-H and C=O vibration modes. The band centered at 1570 cm^{-1} can be attributed to the stretching vibration of H-O-H of the absorption of H_2O molecules [28]. Additionally, two strong peaks centered at about 560 cm^{-1} and 439 cm^{-1} represent the vibration modes of metal-oxygen bonds (Mn-O and Fe-O) at octahedral sites [29].
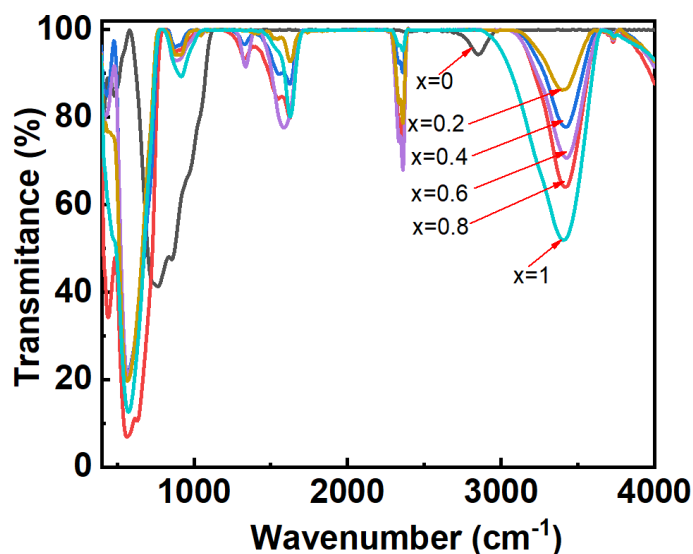
Figure 4. FTIR spectra of $Fe_2Fe_{1-x}Mn_xO_4$.

Similar results were also reported in the previous papers [30]. From Figure 4, it can be found that the characteristic vibration modes of the metal-oxygen shift to low wavenumber, and the intensity of absorption peaks increases gradually when the concentration of Mn^{2+} ions increases, indicating that Fe^{2+} ions were substituted by Mn^{2+} in the Fe-O bonds of the Fe_3O_4 material. The absorption intensity at the peak of 439 cm^{-1} decreased sharply for samples with a Mn^{2+} concentration larger than 0.4. This phenomenon can be explained by the fact that the $MnFe_2O_4$ material belongs to the mixed spinel type, i.e., Mn^{2+} and Fe^{2+} ions occupied both tetrahedral (A) and octahedral (B) positions [31]. When the concentration of Mn^{2+} ions increased, the Mn^{2+} ions were mainly located in the tetrahedral position, so the absorption strength was reduced.

Figure 5 shows the SEM images of the substituted $Fe_2Fe_{1-x}Mn_xO_4$ samples with Mn^{2+} ions at the values of x equal to 0, 0.2, 0.4, 0.6, 0.8 and 1. The SEM image shows that the particles are uniformly spherical in shape with different diameters corresponding to each doping ratio. The pristine Fe_3O_4 material shows the smallest particle size - about 9 nm (Table 1) and increases as the substituted concentration of Mn^{2+} ions in the sample system increases. The ionic radius of Fe^{2+} ion (0.64 Å) is smaller than the ionic radius of Mn^{2+} (0.8 Å). Therefore, replacing Fe^{2+} ions with Mn^{2+} ions will reduce the size of the crystal, leading to an increase in the size of the

particles. This result is consistent with the crystalline size obtained from XRD analysis, demonstrating that the spinel ferrite nanoparticle grains are a single crystal. Besides, the SEM image also confirms that the particles have the phenomenon of agglomeration because they are attracted to each other by the magnetic force.
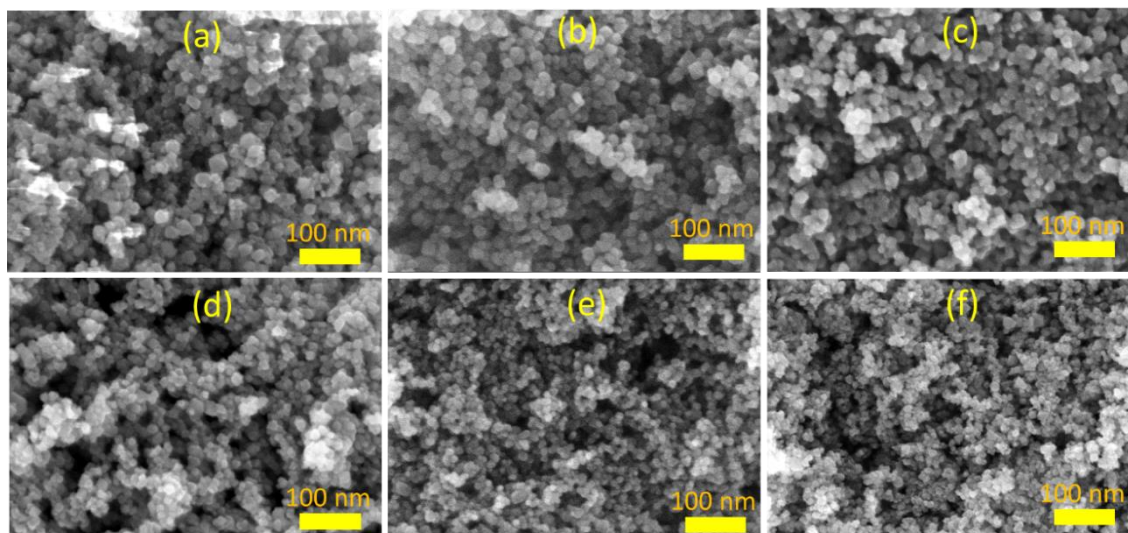
Figure. 5. SEM images of (a) MnFe$_2$O$_4$, (b, c, d, e) Fe$_2$Fe$_{1-x}$Mn$_x$O$_4$ (x = 0.8, 0.6, 0.4 and 0.2) and (f) Fe$_3$O$_4$.

3.2. Magnetic properties of materials
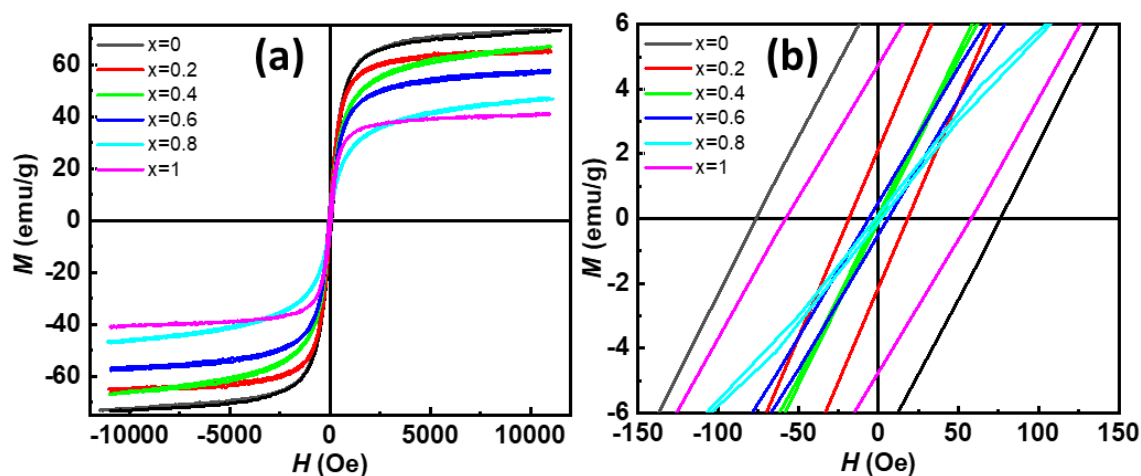
Figure. 6. *(a)* Magnetization curves of the Fe$_2$Fe$_{1-x}$Mn$_x$O$_4$ (x = 0 ÷ 1) and (b) the enlarged low-field hysteresis.

Magnetic properties of Fe$_2$Fe$_{1-x}$Mn$_x$O$_4$ (x = 0 - 1) were studied by the magnetic hysteresis loops measured with the magnetic field in the range from -12 kOe to 12 kOe as shown in Figure 6. From Figure 6, it can be seen that all samples present the soft ferromagnetic properties with the coercivity below 100 Oe (as shown in Figure 6b), indicating a closeness to superparamagnetic behavior.
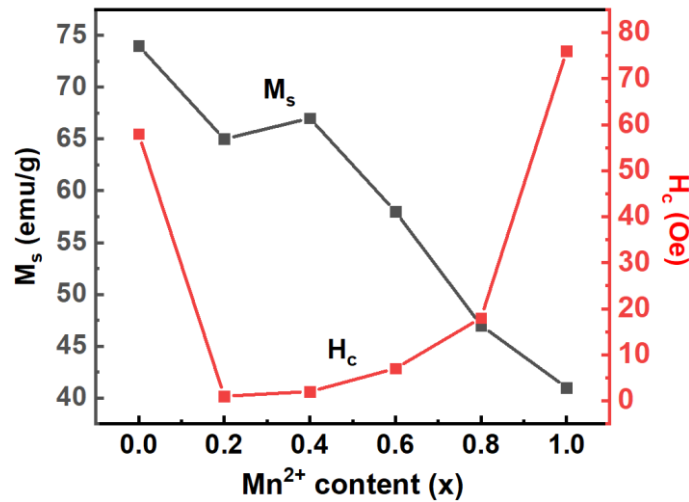
Figure 7. Variation of Ms and H_c with the Mn^{2+} substituted content.

The saturation magnetization (*Ms*) of all samples was estimated by extrapolating the magnetization to high-field regions using the following function:

$$M = M_S(1-\alpha/H) \quad (1)$$

in which α is the fitting parameter. The obtained saturated magnetization and coercivity for all samples are listed in the Table 1 and the variation of Ms and Hc with the Mn^{2+} substituted content is presented in Figure 7.

The highest magnetization of 74 emu/g was observed for the Fe_3O_4 sample and decreased with an increase in the Mn^{2+} substituted concentration. However, the $Fe_2Fe_{1-x}Mn_xO_4$ sample with x = 0.4 displays M_S value which does not obey the trend of decreasing M_S with increasing the Mn^{2+} doping concentration. This can be explained by the fact that the occupation of A site for Mn^{2+} ions forms a mixed spinel structure of the samples with x = 0.4. In the spinel structure, the A and B sublattices are antiferromagnetically coupled when Mn^{2+} ions with the larger ion radius would prefer to occupy the A-site to replace Fe^{3+} ions. This reduces the magnetic moment of the A-site and consequently increases the net magnetization [32]. It is noted that the sample with x = 0.4 remains the Ms value.

The saturation magnetic moment tends to decrease as the doping concentration increases. The reason can be derived from the distribution of Mn^{2+} and Fe^{2+} cations between the sublattice [33].

When Fe^{2+} ions were replaced by Mn^{2+} ions in the crystal, the following cases would occur:

i) When the Mn^{2+} ion replaces the position of the Fe^{2+} ion in sublattice A, the magnetic moment of the sample will increase. Since the magnetic moment of Fe^{2+} (4.9 BM) is smaller than that of Mn^{2+} ion (5.9 BM), the total magnetic moment of the two sublattices increases.

ii) When the Mn^{2+} ion replaces the position of the Fe^{2+} ion in sublattice B, the magnetic moment of the sample will decrease. Because the magnetic moment of the Fe^{2+} ion is smaller than that of the Mn^{2+} ion, the total magnetic moment of the two sublattices decreases.

462

iii) When the Mn^{2+} ion replaces the position of the Fe^{2+} ion in both sublattices A and B, the magnetic moment of the sample will be caused to change, leading to the total magnetic moment of the two sublattice change.

The Ms value tends to decrease because most of the Mn^{2+} ions have replaced Fe^{2+} ions in sublattice B, which is consistent with the results of previous studies [34, 35]. Therefore, the material structure is more mixed than the inverse spinel structure.

In order to investigate the magnetic stability over time of the fabricated samples, M(H) measurements of the samples with x = 0 and x = 0.4 were performed again after two months of synthesis. It is noted that the samples with x = 0 and 0.4 possess the highest M_S value among the substituted samples. The results are shown in Figure 8. It can be seen that after two months of synthesis, the sample with x = 0.4 remained at the Ms value of 67 emu/g while Ms of Fe_3O_4 was reduced by 20 % for the same time. It can be explained by its mixed spinel structure with the substitution of Mn^{2+} on both sides which prevents the substituted sample from oxidizing over time. Thus, the sample with x = 0.4 was chosen as the absorbent for removing DR79.
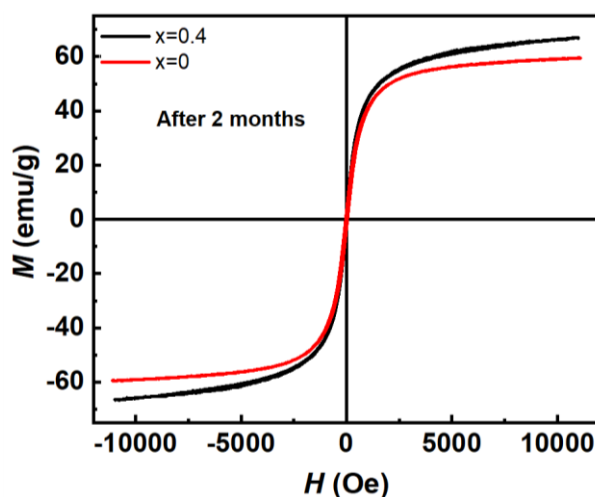
Figure 8. M(H) curves of samples with x = 0 and x = 0.4 after two months of synthesis.

3.3. DR79 adsorption properties of Fe₂Fe₁₋ₓMnₓO₄ x = 0.4 (FMO) material

3.3.1. Isoelectric point of material

50 mg of FMO material was immersed in solutions of different initial pH_i (from 1 to 7). After 24 hours, the solutions were filtered, followed by measuring their pH value (pHe). The difference between the initial pH (pH_i) and the equilibrium pH (pH_e) is $\Delta pH = pH_i - pH_e$, plotting the dependence of ΔpH on pH_i, the intersection point of the curve with the coordinates at which the value ΔpH is the isoelectric point as shown in Figure 9. The results show that the isoelectric point FMO is 6.36. This result indicates that at pH < 6.37, the material's surface is negatively charged, whereas at pH > 6.37, the material's surface is positively charged.
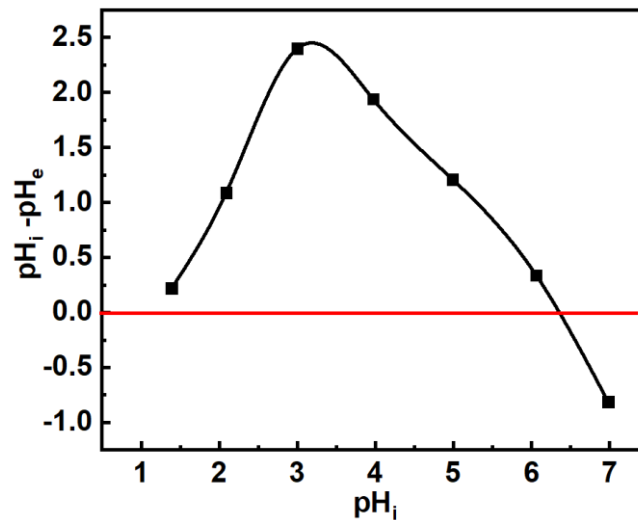
Figure 9. Determination of isoelectric point of FMO.

3.3.2. Effect of initial pH

The pH environment for adsorption is one of the most important factors because it is directly related to the adsorbent surface charge, the adsorbent dissociation, and adsorbent ionization. In this study, the initial pH range from 2 to 7 was investigated. As can be seen in Figure 10, with an initial DR79 concentration of 50 mg/L, FMO weight of 0.02 g, and shaking speed of 300 rpm, pH strongly affects the DR79 adsorption capacity of FMO. The adsorption capacity was strong at pH 2 and rapidly reduced at pH 3, and almost no adsorption took place at higher pH. It can be explained that DR 79 contains many sulfonate radicals ($-SO_3Na$) and amine groups ($-NH_2$), so at low pH, it is protonated as a positively charged molecule. This result is consistent at low pH; the surface of the negatively charged FMO material increases the adsorption capacity of the material at low pH.
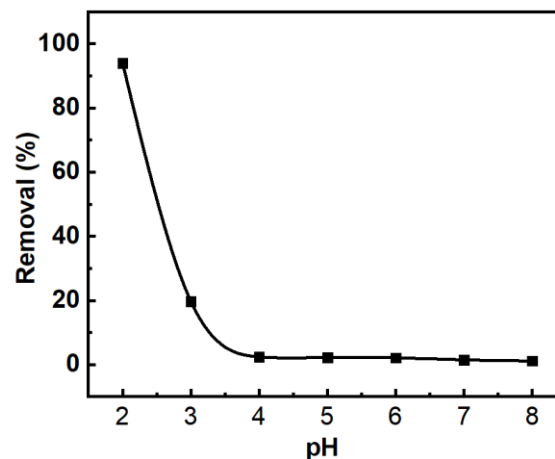
Figure 10. Effect of initial pH on adsorption (50 mg/L DR79; 0.02 g of FMO; 300 rpm).

3.3.3. Effect of absorption time

After a period of adsorption, the adsorption process will reach equilibrium. The evaluation of the adsorption process over time with different amounts of FMO is shown in Figure 11. It can be seen that the adsorption efficiency increased gradually over time and remained almost constant after 70 minutes for all 3 cases. Therefore, a time interval of 70 minutes was chosen as the time for the adsorption to reach equilibrium.
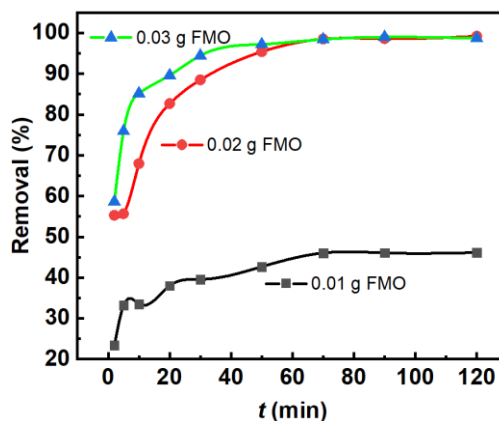
Figure 11. Adsorption efficiency versus time with adsorbent doses of 0.01 g; 0.02 g and 0.03 g.

3.3.4. Effect of adsorbent dose

Various amounts of adsorbent samples ranging from 0.005 g to 0.05 g were added to 50 mL of 50 mgL^{-1} DR79 solutions to study the adsorption process. As shown in Figure 12, the adsorption dye percentage reached above 96 % and tended to increase slowly at a higher initial dosage. This result indicates that there was active center saturation on the absorption surface. However, the adsorption capacity decreased from 183.99 to 48.02 (mg/g).
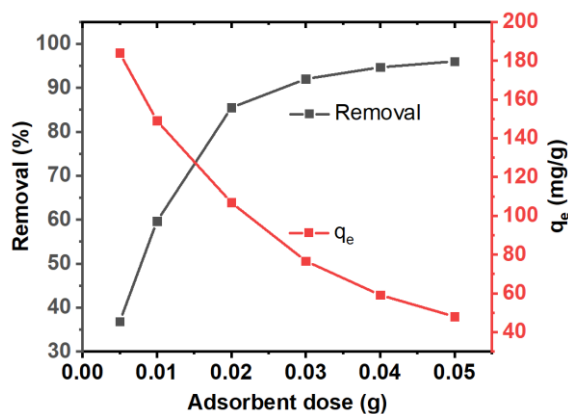
Figure 12. Effect of adsorbent dose (C$_o$ = 50 mg/L; 300 rpm; pH = 2; 25 ^{o}C).

3.3.5. Adsorption isotherms

Based on the adsorption process with different adsorbent doses, adsorption isotherm models can be found.
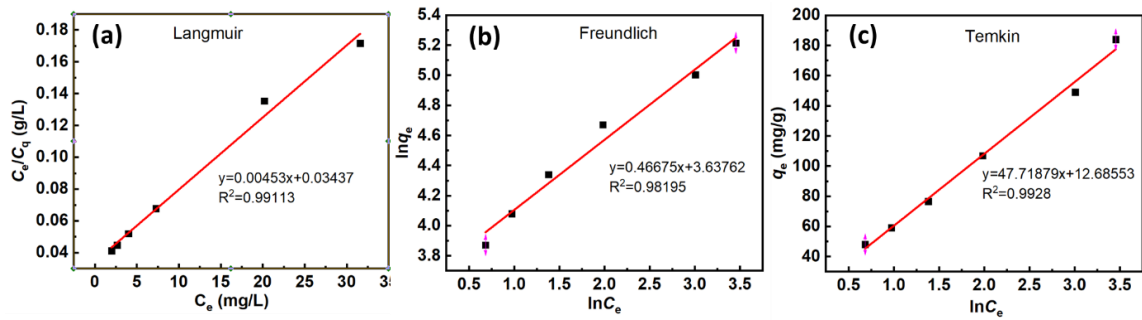
Figure 13. Adsorption isotherms: (a) Langmuir, (b) Freundlich, and (c) Temkin models.

Table 2. Constants of Langmuir, Freundlich and Temkin models.

Langmuir	$q_{max} = 220.75$	$K_L = 0.1318$	$R^2 = 0.99113$
Freundlich	$\dfrac{1}{n} = 0.46675$	$K_F = 38.00$	$R^2 = 0.98195$
Temkin	$A_t = 1.305$	$b_t = 51.92$ (J.mol^{-1})	$R^2 = 0.9928$

A study of isotherm adsorption models is shown in Figure 13. The constants and correlation coefficients are calculated and shown in Table 2. It can be seen that the above adsorption models are quite suitable in which the Temkin isothermal adsorption model shows the best fit from the actual values ($R^2 = 0.9928$) [36].

3.3.6. Adsorption kinetics
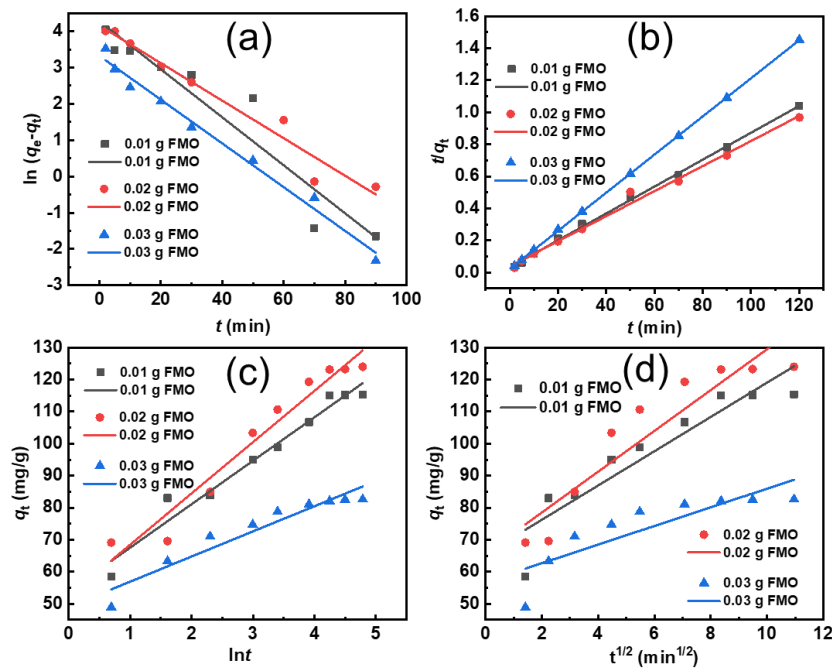
Figure 14. Adsorption kinetics: (a) Pseudo-first-order; (b) Pseudo-second-order constants; (c) Elovich constants; and (d) Intra-particle diffusion.

Table 3. Kinetic parameters.

Adsorbent dose (g)	Pseudo-first-order constants			Pseudo-second-order constants		
	q_e (mg/g)	k_1	R^2	q_e (mg/g)	k_2	R^2
0.01	71.833	0.06611	0.91256	119.05	0.002183	0.99861
0.02	63.90	0.05171	0.96378	127.88	0.001587	0.99224
0.03	27.70	0.06026	0.9864	83.96	0.006564	0.99995
	Elovich constants			Intra-particle diffusion constants		
	α	β	R^2	K_p	C	R^2
0.01	724.2368	0.073719	0.96435	5.3498	65.546	0.86201
0.02	423.5824	0.062466	0.95224	6.3723	65.773	0.86709
0.03	4074.877	0.127436	0.91901	2.9093	56.852	0.72599

The adsorption kinetics was investigated according to various models as shown in Figure 14. Kinetic parameters are shown in Table 3. It can be seen that the correlation coefficient (R^2) for the second-order kinetic model is the largest ($R^2 > 0.992$), much larger than the first-order model ($R^2 < 0.964$), Elovich model ($R^2 < 0.965$), and Intra-particle diffusion model (very low, $R^2 < 0.868$).

4. CONCLUSIONS

The substituted products Fe$_2$Fe$_{1-x}$Mn$_x$O$_4$ (x = 0 - 1) were successfully synthesized by the co-precipitation method. The obtained samples display a cubic spinel structure with particle sizes ranging from 9 to 40 nm depending on the substituted concentration of Mn^{2+}. The lattice constant and particle size increase with increasing the Mn^{2+} substitution. Especially, FTIR and magnetization results reveal that at high substituted Mn^{2+} concentrations, the samples exhibit a mixed spinel structure. As a consequence, the magnetization values of the samples depend strongly on the cation distribution. The existence of the mixed spinel structure helps the samples with x = 0.4 maintain their saturation magnetization after two months. The DR79 adsorption study of Fe$_2$Fe$_{1-x}$Mn$_x$O$_4$ (x = 0.4) materials showed that the adsorption of the materials was high at low pH (at pH = 2) and decreased very quickly at higher pH. At pH 2, the time to reach adsorption equilibrium was 60 min. The experimental data show that the adsorption process is quite suitable with Langmuir, Freundlich, and Tempkin models, in which the Temkin model gives the best fit. The adsorption kinetics is ideal for the pseudo-second-order adsorption model.

CRediT authorship contribution statement. Pham Hoai Linh: Formal analysis, Supervision, Funding acquisition. Nguyen Quoc Dung: Formal analysis, Methodology, Investigation. Nguyen Van Khien: Formal analysis, Investigation.

Declaration of competing interest. The authors declare that they have no known competing financial interests or personal relationships that could have appeared to influence the work reported in this paper.

REFERENCES

1. Zhang H., Hou A., Xie K., Gao A. - Smart color-changing paper packaging sensors with pH sensitive chromophores based on azo-anthraquinone reactive dyes, Sensors and Actuators B: Chemical. **286** (2019) 362-369. https://doi.org/10.1016/j.snb.2019.01.165

2. GilPavas E., Dobrosz-Gómez I., Gómez-García M. Á. - Optimization and toxicity assessment of a combined electrocoagulation, $H_2O_2/Fe^{2+}/UV$ and activated carbon adsorption for textile wastewater treatment, Science of the Total Environment. **651** (2019) 551-560. https://doi.org/10.1016/j.scitotenv.2018.09.125

3. Ozturk E., Koseoglu H., Karaboyacı M., Yigit N. O., Yetis U., Kitis M. - Minimization of water and chemical use in a cotton/polyester fabric dyeing textile mill. Journal of cleaner production. **130** (2016) 92-102. https://doi.org/10.1016/j.jclepro.2016.01.080

4. Ziane S., Bessaha F., Marouf-Khelifa K., Khelifa A. - Single and binary adsorption of reactive black 5 and Congo red on modified dolomite: Performance and mechanism, Journal of Molecular Liquids. **249** (2018) 1245-1253. https://doi.org/10.1016/j.molliq.2017.11.130

5. Mahmoodi N. M., Arami M., Bahrami H., Khorramfar S. - The effect of pH on the removal of anionic dyes from colored textile wastewater using a biosorbent, Journal of applied polymer science. **120** (2011) 2996-3003. https://doi.org/10.1002/app.33406

6. Anastopoulos I., Kyzas G. Z. - Agricultural peels for dye adsorption: a review of recent literature, Journal of Molecular Liquids. **200** (2014) 381-389. https://doi.org/10.1016/j.molliq.2014.11.006

7. Kozakova Z., Klimova E. J., Obradovic B. M., Dojcinovic B. P., Krcma F., Kuraica M. M., Olejnickova Z., Sykora R., Vavrova M. - Comparison of liquid and liquid-gas phase plasma reactors for discoloration of azo dyes: Analysis of degradation products, Plasma Processes and Polymers. **15** (2018) 1700178. https://doi.org/10.1002/ppap.201700178

8. Kavcı E. - Adsorption of Direct Red 243 dye onto clay: Kinetic study and isotherm analysis, Desalination and Water Treatment. **212** (2021) 452-461. https://doi.org/10.5004/dwt.2021.26861

9. Worch E. - Adsorption Technology in Water Treatment Fundamentals, Processes, and Modeling. Walter de Gruyter GmbH & Co. KG Berlin/Boston, 2012

10. Balarak D., Zafariyan M., Igwegbe C. A., Onyechi K. K., Ighalo J. O. - Adsorption of acid blue 92 dye from aqueous solutions by single-walled carbon nanotubes: isothermal, kinetic, and thermodynamic studies. Environmental Processes. **8** (2021) 869-888. https://doi.org/10.1007/s40710-021-00505-3

11. Velusamy S., Roy A., Sundaram S., Kumar Mallick T. - A review on heavy metal ions and containing dyes removal through graphene oxide-based adsorption strategies for textile wastewater treatment. The Chemical Record. **21** (2021) 1570-1610. https://doi.org/10.1002/tcr.202000153

12. Grimm O. C., Somaratne R. D. S., Wang Y., Kim S., Whitten J. E. - Thiol adsorption on metal oxide nanoparticles, Physical Chemistry Chemical Physics. **23** (2021) 8309-8317. https://doi.org/10.1039/D1CP00506E

13. Gómez-Pastora J., Bringas E., Ortiz I. - Recent progress and future challenges on the use of high performance magnetic nano-adsorbents in environmental applications, Chem. Eng. J. **256** (2014) 187-204. https://doi.org/10.1016/j.cej.2014.06.119

14. John Zhang Z. Z. L., Wang., Bryan C. Chakoumakos and Jin S. Yin - Temperature Dependence of Cation Distribution and Oxidation State in Magnetic Mn-Fe Ferrite Nanocrystals, Journal of American Chemical Society. **120** (1998) 1800-1804. https://doi.org/10.1021/ja973085l

15. Harikishore D., Reddya K., Yun Y. S. - Spinel ferrite magnetic adsorbents: alternative future materials for water purification, Coordination Chemistry Reviews. **315** (2016) 90-111. https://doi.org/10.1016/j.ccr.2016.01.012

16. Tang S. C. N., Lo I. M. C. - Magnetic nanoparticles: Essential factors for sustainable environmental applications, Water Research. **47** (2013) 2613 e2632. https://doi.org/10.1016/j.watres.2013.02.039.

17. Wei X., Bhojappa S., Lin L.-S., Viadero R. C. - Performance of Nano-magnetite for removal of selenium from aqueous solutions, Environ. Eng. Sci. **29** (6) (2012) 526-532. https://doi.org.10.1089/ees.2011.0383

18. KumarReddy D. H., Yeoung-SangYun - Spinel ferrite magnetic adsorbents: Alternative future materials for water purification, Coordination Chemistry Reviews. **315** (2016) 90-111. https://doi.org/10.1016/j.ccr.2016.01.012

19. Jozef Slama, Martin Soka, Gruskova A., Rastislav Dosoudil, Vladimır Jancˇa'rik, Degmova' J. - Magnetic properties of selected substituted spinel ferrites, JournalofMagnetismandMagneticMaterials. **32** (2013) 6251-6256. https://doi.org/10.1016/j.jmmm.2012.07.016

20. Araújo C. S., Almeida I. L., Rezende H. C., Marcionilio S. M., Léon J. J., de Matos T. N. - Elucidation of mechanism involved in adsorption of Pb (II) onto lobeira fruit (Solanum lycocarpum) using Langmuir, Freundlich and Temkin isotherms, Microchemical Journal. **137** (2018) 348-354. https://doi.org/10.1016/j.microc.2017.11.009

21. 21.Afsar M. Z., Hoque S., Osman K. - A comparison of the Langmuir, Freundlich and Temkin equations to describe phosphate sorption characteristics of some representative soils of Bangladesh, International Journal of Soil Science. **7** (2012) 91. https://doi.org/10.3923/ijss.2012.91.99

22. Kajjumba G. W., Emik S., Öngen A., Özcan H. K., Aydın S. - Modelling of adsorption kinetic processes-errors, theory and application, In Advanced Sorption Process Applications, Edebali, S., Ed., InTech Open Limited: London, UK, 2019, pp. 1-19.

23. Li Z., Gao K., Han G., Wang R., Li H., Zhao X., Guo P. - Solvothermal synthesis of MnFe$_2$O$_4$ colloidal nanocrystal assemblies and their magnetic and electrocatalytic properties, New Journal of Chemistry. **39** (2015) 361-368. https://doi.org/10.1039/C4NJ01466A

24. Gong J., Lin X. - Facilitated electron transfer of hemoglobin embedded in nanosized Fe$_3$O$_4$ matrix based on paraffin impregnated graphite electrode and electrochemical catalysis for trichloroacetic acid, Microchemical Journal. **75** (2003) 51-57. https://doi.org/10.1016/S0026-265X(03)00053-5

25. Liao M. H., Chen D. H. - Immobilization of yeast alcohol dehydrogenase on magnetic nanoparticles for improving its stability, Biotechnology Letters. **23** (2001) 1723-1727. https://doi.org/10.1023/A:1012485221802

26. Gul I., Abbasi A., Amin F., Anis-ur-Rehman M., Maqsood A. - Structural, magnetic and electrical properties of $Co_{1-x}Zn_xFe_2O_4$ synthesized by co-precipitation method, Journal of magnetism and magnetic materials. **311** (2007) 494-499. https://doi.org/10.1016/j.jmmm.2006.08.005

27. Freire R., Ribeiro T., Vasconcelos I., Denardin J. C., Barros E., Mele G., Carbone L., Mazzetto S., Fechine P. - $MZnFe_2O_4$ (M = Ni, Mn) cubic superparamagnetic nanoparticles obtained by hydrothermal synthesis, Journal of nanoparticle research. **15** (2013) 1-12. https://doi.org/10.1007/s11051-013-1616-3

28. Wang M., Shao C., Zhou S., Yang J., Xu F. - Preparation of carbon aerogels from TEMPO-oxidized cellulose nanofibers for organic solvents absorption, RSC Advances. **7** (2017) 38220-38230. https://doi.org/10.1039/C7RA05506D

29. Zhou Y., Xiao B., Liu S. Q., Meng Z., Chen Z. G., Zou C. Y., Liu C. B., Chen F., Zhou X. - Photo-Fenton degradation of ammonia via a manganese–iron double-active component catalyst of graphene-manganese ferrite under visible light, Chemical Engineering Journal. **283** (2016) 266-275. https://doi.org/10.1016/j.cej.2015.07.049

30. Zipare K., Dhumal J., Bandgar S., Mathe V., Shahane G. - Superparamagnetic manganese ferrite nanoparticles: synthesis and magnetic properties, Journal of Nanoscience and Nanoengineering. **1** (2015) 178-182.

31. Cullity B. D., Graham C. D. - Introduction to magnetic materials, Second Edition, John Wiley & Sons, New York, 2008

32. Xin Liu, Liu J., Zhang S., Nan Z., Shi Q. - Structural, Magnetic, and Thermodynamic Evolutions of Zn-Doped Fe_3O_4 Nanoparticles Synthesized Using a One-Step Solvothermal Method, J. Phys. Chem. C. **120** (2016) 1328-1341. https://doi.org/10.1021/acs.jpcc.5b10618

33. Islam K., Haque M., Kumar A., Hoq A., Hyder F., Hoque S. M. - Manganese ferrite nanoparticles ($MnFe_2O_4$): size dependence for hyperthermia and negative/positive contrast enhancement in MRI, Nanomaterials. **10** (2020) 2297. https://doi.org/10.3390/nano10112297

34. Yazdia S.T., Iranmaneshb P., Saeedniac M. M. S. - Structural, optical and magnetic properties of $MnxFe_{3-x}O_4$ nanoferrites synthesized by a simple capping agent-free coprecipitation route, Materials Science & Engineering B. **245** (2019) 55-62. https://doi.org/10.1016/j.mseb.2019.05.009

35. Li M., Gao Q., Wang T., Gong Y. S., Han B., Xia K. S., Zhou C. G. - Solvothermal synthesis of MnxFe3 − xO4 nanoparticles with interesting physicochemical characteristics and good catalytic degradation activity, Materials and Design. **97** (2016) 341-348. http://dx.doi.org/10.1016/j.matdes.2016.02.103

36. Han R., Ma J., Yang C., Cui T., Liu W., Wang S. - Synthesis of nitrogen-doped carbon nanocages for sensitive electrochemical detection of uric acid, Materials Letters. **255** (2019) 126520-126520. https://doi.org/10.1016/j.matlet.2019.126520